Chapter Five

Magnetic Properties: Discussion

5.1 Overview

Chapter 4 presents measurements of magnetic properties for b-axis-oriented Dy, obtained via SQUID magnetometry. Nearly all observed magnetic properties differ significantly from c-axis-oriented thin film Dy and from bulk Dy. This confirms that the reduction of symmetry has important consequences for systems with strong, symmetry-dependent properties. The present Chapter specifically addresses these differences to show how they can be understood in terms of basic magnetic interactions. It begins with a discussion of magnetic anisotropy, since this contains essential ingredients for an interpretation of the magnetic phase diagram. Next, the ferromagnetic/anti-ferromagnetic phase transition is discussed. It is shown that the phase behavior of b-axis-oriented, c-axis-oriented, and bulk Dy can be understood by a single model which is dominated by the known magnetoelastic constants of bulk Dy. The remaining Sections discuss other significant experimental observations. These include the observed critical fields, the coercivities and domain wall pinning, and the reduction of Néel temperature from that of bulk Dy. Finally, magnetic relaxation measurements are discussed.

5.2 Magnetic Anisotropy

Magnetic anisotropy causes the magnetic moments to prefer specific crystallographic directions. Magnetization is more readily achieved by a small applied field along an "easy" direction, and conversely it is less readily achieved by the same field applied along

a "hard" direction. In bulk Dy, the easy magnetization axes are the six equivalent [11$\bar{2}$0] directions and the [0001] axis is the hard axis. The results of Chapter 4 show that for a field applied along the in-plane a-axis, the hysteresis loops change shape from square to diagonal as the strain changes from tensile to compressive. For a field applied along the out-of-plane b-axis, almost the opposite effect is seen; in the case of compressive strain, however, the hysteresis loops are less square. The interpretation provided there has the in-plane a-axis becoming an increasingly easy axis for increasing tensile strain and an increasingly hard axis for compressive strain. For compressive strain the easy axis changed from the in-plane a-axis to favor the two out-of-plane a-axes.

A superposition of the anisotropy effects presented in Chapter 1 can be used to understand this behavior. The relevant magnetoelastic Hamiltonian that gives the total energy of ferromagnetic Dy is

$$H = H_{CF} + H_{ME} + H_S + H_Z . \tag{5.1}$$

This includes 1) H_{CF}, the magnetocrystalline anisotropy, which derives from the electrostatic potential and depends on the point symmetry of the Dy lattice [1]; 2) H_{ME}, the magnetoelastic energy, which couples the preferred orientation of the moment to elastic distortions; 3) H_S, shape anisotropy, which couples the direction of the magnetic moment to the shape of the crystal, via demagnetization fields generated at the sample boundaries; and 4) H_Z, Zeeman energy, which couples the magnetic moments to the applied field. Each of these terms is explained in Chapter 1.

The magnetic contribution to the energy of thin, strained b-axis-oriented Dy in zero applied field, $H_Z = 0$, is calculated using this Hamiltonian, Eq. (5.1). The results are presented as Figure 5.1, which gives the energy as a function of magnetization direction. Only the basal plane directions are shown since the [0001] axis remains the hard magnetization axis.

Bulk Dy. Magnetocrystalline anisotropy is the only relevant effect so the free energy exhibits the expected sixfold symmetry. The six equivalent [11$\bar{2}$0] directions are the easy magnetization axis.
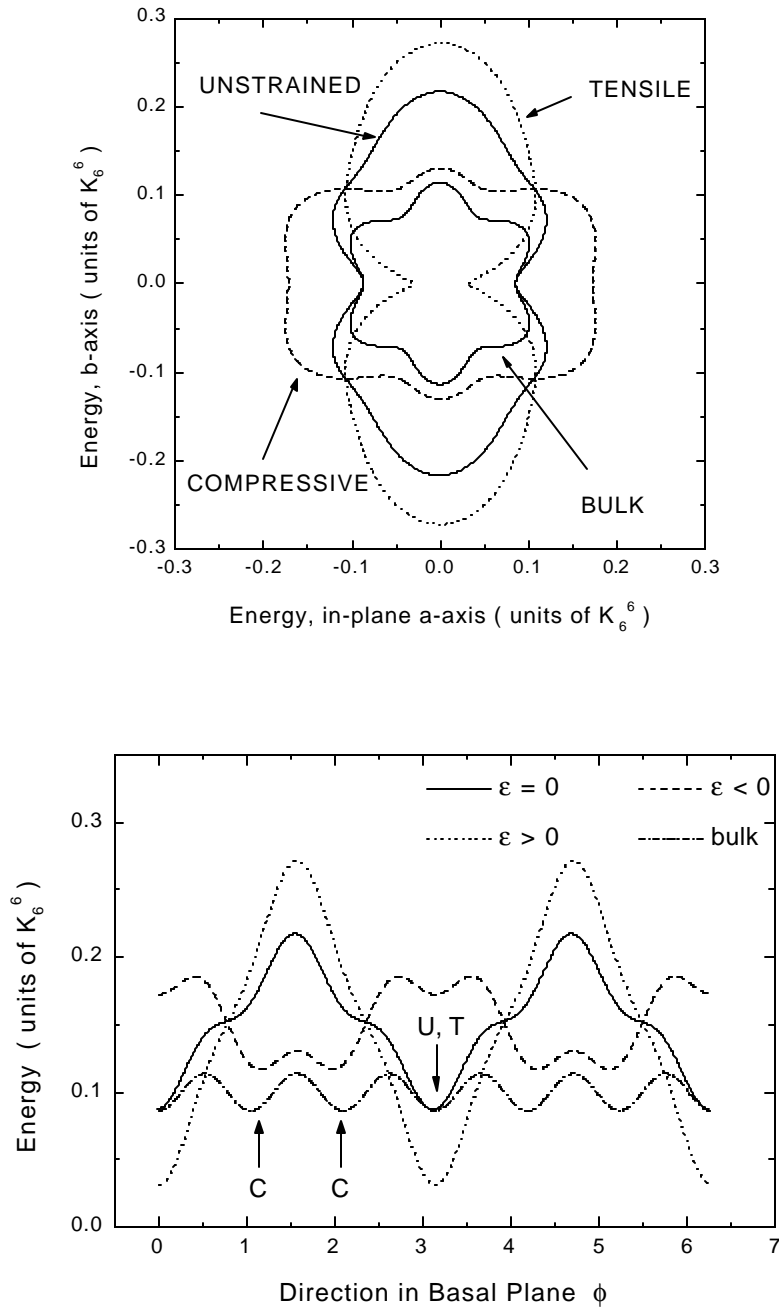
Figure 5.1. (Top) A polar plot of the energy of a magnetic moment in the basal plane of strained, thin, b-axis-oriented Dy, compared with the bulk case. (Bottom) A rectangular plot of the free energy, in which the energy minima for the compressive, unstrained, and tensile cases are identified. The bulk and unstrained cases differ because of shape anisotropy, an important effect.

Unstrained b-axis-oriented Dy. A large difference occurs between bulk Dy and thin unstrained b-axis-oriented Dy owing to the shape anisotropy of the latter. The free energy for the states magnetized along the in-plane [11$\overline{2}$0] axis remains unchanged, and the results show that it becomes less favorable for the moment in a thin film to cant out of the film plane.

Compressed b-axis-oriented Dy. The in-plane [11$\overline{2}$0] direction becomes an increasingly hard magnetization direction for increasing compressive strain. For sufficiently large compressive strains, the in-plane [11$\overline{2}$0] direction no longer remains the easy axis. The magnetoelastic interaction makes it favorable for a Dy moment to cant out of the plane of the film into one of the four equivalent out-of-plane [11$\overline{2}$0] approximate energy minima. A magnetic moment with a perpendicular component is otherwise energetically unfavorable, because of shape anisotropy, but this energy deficit is overcompensated by the reduction in magnetoelastic energy.

Stretched b-axis-oriented Dy. The in-plane [11$\overline{2}$0] axis is now the easy axis and since the energy for this direction decreases with increasing tensile strain it becomes an increasingly easy axis of magnetization. This behavior recalls the magnetostriction of bulk Dy which, upon becoming ferromagnetic, exhibits a spontaneous orthorhombic distortion which lowers the hexagonal symmetry as the lattice elongates and magnetizes along one of the equivalent of the [11$\overline{2}$0] directions [2]. The effect of tensile epitaxial strain in films is to force exactly this type of lattice distortion, thus making the two equivalent in-plane [11$\overline{2}$0] directions the states of lowest energy.

When the Zeeman interaction is added to yield the energy of a Dy moment in a magnetic field applied along the in-plane [11$\overline{2}$0] direction, the results are as shown in Figure 5.2. For all applied fields there is a reduction of energy along the field direction. As the applied field increases, regardless of strain, the in-plane [11$\overline{2}$0] direction eventually becomes the orientation of lowest energy. This is to be expected because for a sufficiently

large field the Zeeman term exceeds all other anisotropic terms and rotates the moments into alignment parallel with the field.

In summary, when the bulk properties of Dy are modified by the anisotropy caused by strain, shape anisotropy and applied field, the results are quantitatively consistent with the experimentally-observed behavior.
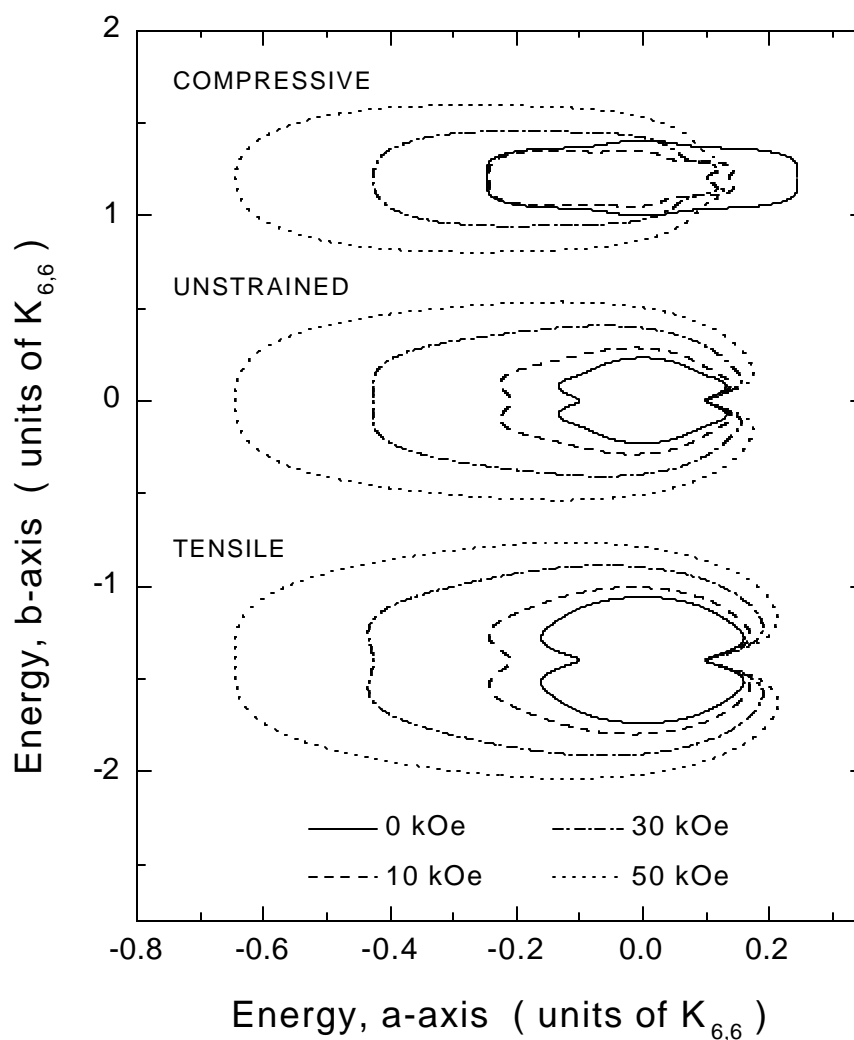

Figure 5.2. Calculated energy of a Dy moment in b-axis-oriented Dy in a field applied along the in-plane a-axis direction. For sufficiently strong fields, the in-plane a-axis becomes the direction of lowest energy, regardless of strain.

5.3 Strain-dependence of Ferromagnetic Ordering, *T*

The magnetic phase diagram of b-axis-oriented Dy, shown as Figure 4.5 of Chapter 4, introduces three important features. First, the lowest observed critical temperature occurs for unstrained Dy at 78 K and this is slightly *lower* than that observed for bulk Dy, 90 K. Second, the critical temperatures increase with increasing strain, both compressive and tensile. Third, the strain dependence of the critical temperature is approximately linear, with the weaker strain dependence on the compressive side. This phase diagram is markedly different from both that of bulk Dy and c-axis-oriented Dy.

This Section provides, for the first time, a calculation of the effect of strain on T_C for b-axis-oriented, c-axis-oriented, and bulk Dy, using the same approach and material-dependent parameters for all cases. The calculation initially follows the model developed by Erwin, in which the elastic and magnetoelastic energies for the thin film cases are calculated using the parameters from bulk Dy. In the present case, however, the calculation is extended to obtain the temperature-dependence of T_C. The material is organized in the following way. First, the magnetoelastic energy difference between the ferromagnetic and antiferromagnetic phases of Dy is calculated. Next, this energy difference is connected to the T_C by means of the Gibbs free energy. Finally, important physical parameters such as the latent heat are determined by fitting the Gibbs function to the data.

Calculation of Magnetoelastic Energy

Calculations of the magnetoelastic energy difference between the FM and AF states for the FM/AF phase transition in bulk and thin film Dy are reviewed in Chapter 1. It was suggested by Cooper in 1967 that the driving energy derived principally from the lowest-order magnetoelastic terms associated with the reduction of cylindrical symmetry [3],[4]. This model was improved by Evenson and Liu, who wrote an expression for the driving energy which involved the approximate exchange energy in the AF state [5]. Dumesnil and co-workers used experimental measurements of turn angle to model the phase

diagram of c-axis-oriented Dy [6]. Unfortunately, while the qualitative ideas by Cooper remain valid, the simplified description of the long-range exchange mechanism employed in later work undermines the specific results reported by Evenson and Liu and used by Dumesnil and co-workers.

In any event, an application of this formalism to b-axis-oriented Dy is problematic for several other reasons. Most significantly, there are as yet no measurements of the magnetic periodicity of the AF state. The hexagonal symmetry is broken, therefore the helical structure (normally observed in bulk and in c-axis-oriented thin films) may reasonably be expected to contain higher-order Fourier components, due both to the symmetry-breaking of the magnetoelastic interaction as well as demagnetization forces from the periodic component of magnetization normal to the film plane. In fact, since b-axis-oriented thin films are not clamped against out-of-plane distortions [7], a periodic lattice distortion near the surface may result, similar to that which accompanies the charge-density-waves in Cr [8].

For these reasons a phenomenological calculation of the type first employed by Erwin offers considerable advantages [9],[10]. This method was first applied to explain the observed suppression of T_C in strained, epitaxial c-axis-oriented rare earths. It is an accurate model because the magnetoelastic coefficients are fitted to the measured equilibrium strains of the bulk material. The calculation involves two parts: 1) the elastic and magnetoelastic energies are calculated for the AF and FM states using the actual strains appropriate for the specific cases. The exchange energies of the AF and FM states are not known but are represented here by the first terms of Taylor expansions in the strain. The results are augmented to include shape anisotropy, which for compressed b-axis-oriented Dy is a significant contribution. The calculation allows the exchange interaction term to be inferred from a fit to the experimental results, thereby affording a first determination of its variation with orthogonal strains.

The magnetoelastic energy is calculated from the elastic energy, quadratic in strains, which shifts to a new equilibrium value through the addition of a magnetic term (linear in strain). From first principles, Callen and Callen show that the magnetic free energy is a

linear perturbation that derives from the single-ion (magnetoelastic) and two-ion (exchange) mechanisms, Eq. (1.18). From a wider perspective, however, one can *always* expand the dominant exchange and magnetocrystalline terms in a Taylor series involving strain, without regard to interaction-specific details [11]. The magnetoelastic energy is

$$E = E_{\text{elas}} + E_{\text{me}}$$
$$= \frac{1}{2} \sum_{m,n} c_{mn} e_{mm} e_{nn} - \sum_{m} K_m e_{mm} , \tag{5.2}$$

where c_i and K_i have numerical values obtained from bulk Dy; these are tabulated in Table 5.1 and 5.2, respectively. Eq. (5.2) is valid for stretched b-axis-oriented Dy, c-axis-oriented Dy, and bulk Dy under hydrostatic stress uniaxial stress applied along the b and c directions. In these cases, the compression of ε_{22} favors magnetization along $[11\overline{2}0]$. For compressed b-axis-oriented Dy, and bulk Dy under uniaxial stress applied along the $[11\overline{2}0]$ direction, however, ε_{22} is positive and the magnetization is oriented along the canted, out-of-plane $[11\overline{2}0]$ directions. For these cases, the new magnetoelastic constants K_{ii}^{C} are obtained from those for the tensile strain K_{ii}^{T} by a 60⁰ rotation of coordinates,

$$K_{11}^{C} = \frac{1}{\sqrt{3}} K_{11}^{T} - \frac{2}{\sqrt{3}} K_{22}^{T} ,$$
$$K_{22}^{T} = \frac{2}{\sqrt{3}} K_{11}^{T} - \frac{1}{\sqrt{3}} K_{22}^{T} . \tag{5.3}$$

To evaluate the energy, all strains must be known. For the b-axis-oriented and c-axis-oriented cases, the films are both *strained* and *clamped* and Eqs. (5.2) and (5.3) are evaluated using the in-plane strains established by epitaxy. The thin film strains in the unclamped out-of-plane direction are easily calculated using the elastic equations given as Eq. (1.8). For the bulk uniaxial and hydrostatic cases, the strains are obtained from the applied pressure similarly by means of Eq. (1.8). The energies are shown as Figure 5.3, and the differences in energy ($\Delta E = E_{FM} - E_{AF}$) are shown as Figure 5.4. For comparison with measured data (see next Section), the cases considered are b-axis-oriented Dy, c-axis-

134

oriented Dy, and bulk Dy under both uniaxial and hydrostatic stress. Because the elastic contribution does not change between the AF and FM states, the driving energies depend linearly on strain. In what follows, an argument which connects the driving energy linearly with T_C is presented.

Elastic Constant	(J/cm³)
c_{11}	7.0×10^4
c_{12}	1.55×10^4
c_{13}	1.87×10^4
c_{33}	8.35×10^4
c_{44}	2.63×10^4
c_{66}	2.72×10^4

Table 5.1. The elastic constants used in the calculations. These are obtained from the irreducible elastic constants, discussed in Chapter 1.

Coefficient	(J/cm³)	
	FM	AF
K_{11}^T	-7.05×10^{-1}	-1.63×10^2
K_{22}^T	-3.99×10^2	-1.40×10^2
K_{11}^C	4.60×10^2	6.74×10^1
K_{22}^C	-2.31×10^2	-2.68×10^2
K_{33}	2.31×10^2	1.17×10^2

Table 5.2 The magnetoelastic coefficients used in the calculations. These are calculated using x-ray diffraction measurements of the bulk Dy lattice parameters, as discussed in Chapter 1.
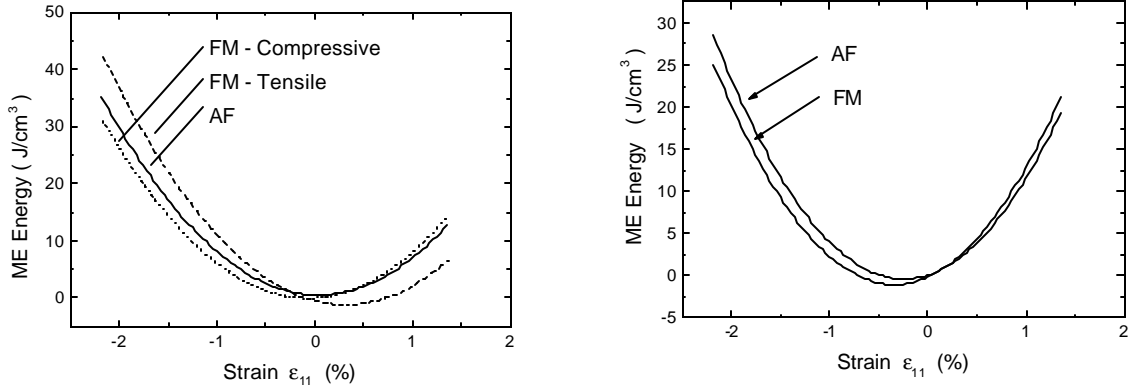
Figure 5.3. The magnetoelastic energy as a function of strain for b-axis-oriented (left) and c-axis-oriented (right) Dy, for the ferromagnetic and helical antiferromagnetic states. The energy of the ferromagnetic state is lower for tensile strain, as expected qualitatively from knowledge of the type of orthorhombic distortion which accompanies ferromagnetism.
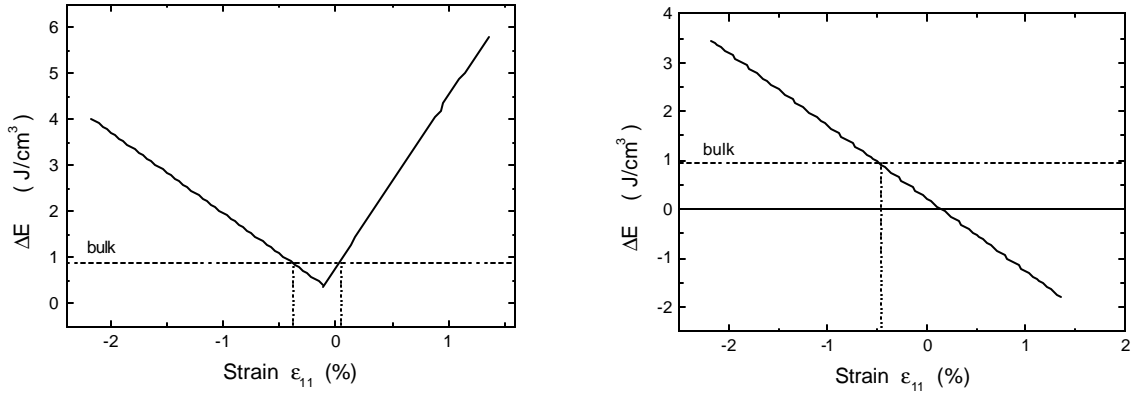

Figure 5.4: The magnetoelastic driving energy as a function of strain for b-axis-oriented (left) and c-axis-oriented (right) Dy. The driving energy for bulk Dy (0.94 J/cm³) is shown as a dotted line.
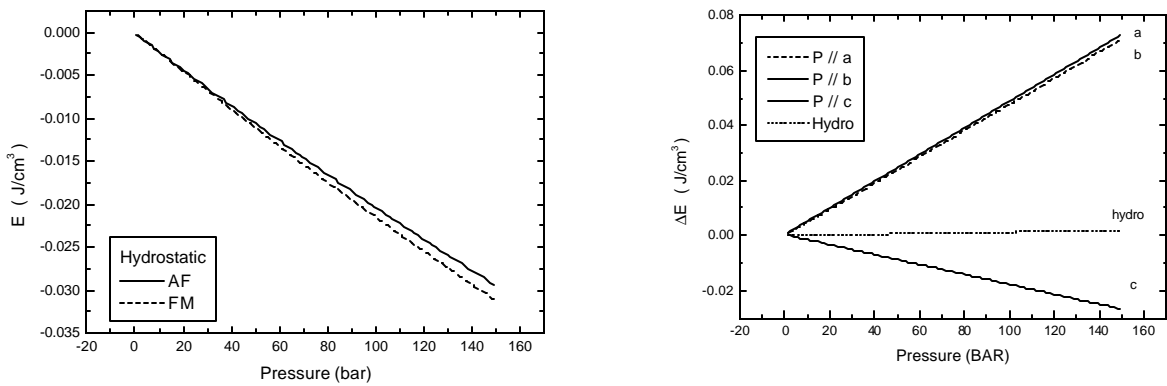

Figure 5.5. (Left) The magnetoelastic energy for bulk Dy under hydrostatic stress. (Right) The difference in magnetoelastic energy for bulk Dy under uniaxial and hydrostatic stress.

Relationship Between T_C and Driving Energy

The previous Section shows that the difference in magnetoelastic energy between the FM and AF states varies linearly with strain. In a study of Er using this magnetoelastic model, Borchers found a similar linear relationship: the ferromagnetic transition of Er grown on Y was supressed in zero field, but the magnetoelastic energy could be related linearly to the energy equivalent of the critical field at different temperatures using the Zeeman interaction, in good agreement with experiment [12]. This Section addresses, for the first time, whether this linear behavior is reasonable.

Until now, the entropic contribution to the free energy has been neglected. The *total* free energy (including elastic, magnetoelastic, and entropy terms) is

$$F = E + E_0 - TS , \qquad (5.4)$$

where T is temperature and S is entropy, which is comprised on lattice and magnetic contributions. The zero point energy E_0 of each state is non-trivial; this has been discussed for the rare earths by Egami [13]. The transition between the FM and AF states is first order, therefore $\Delta F = 0$ at $T = T_C$ and Eq. (5.4) becomes

$$T_C = \frac{1}{\Delta S}(\Delta E_0 + \Delta E(\boldsymbol{e})) \qquad (5.5)$$

where ΔE_0 is the enthalpy of formation (latent heat) of the phase transition. This assumes that the entropy difference at T_C does not depend on temperature. Since there is no strong temperature-dependence of the magnetic degrees of freedom in the FM or AF state at T_C, this approximation is reasonable. Eq. (5.5) thus provides the required *linear* connection between the driving energy and temperature.

A first principles calculation of the variation of T_C with strain requires that all terms in Eq. (5.5) be known. Unfortunately, the exact numerical dependence of the exchange energy ΔE_{EX} on strain and the shape anisotropy E_S for compressed b-axis-oriented Dy are not known. However, both T_C vs. strain (from experiment) and ΔE_{ME} vs. strain (from calculation) are known. Further, it is reasonable from Eq. (1.19), or otherwise by Taylor expansion, that ΔE_{EX} depends linearly on strain for small strains. Since the FM/AF phase

transition is first order and the Gibbs free energies must be equal ($\Delta F = 0$) at the transition, the measured T_C and calculated ΔE_{ME} can be used in a fitting scheme to experimentally determine the strength of ΔE_{EX} and E_S.

This thesis work provided measurements of T_C vs. strain for b-axis-oriented Dy. In addition, there are results from Tsui and Flynn for c-axis-oriented Dy [14] and Bartholin for bulk Dy (under hydrostatic stress, and under uniaxial stress for both a spherical and a cubic sample [15]). The results of the present fitting for these cases are presented in Table 5.3, and the calculated temperatures and energies appear in Figures 5.6, 5.7, and 5.8. Further details are now given for each of the cases considered.

b-axis-oriented Dy. For compressed Dy, the shape anisotropy is calculated to be -0.35 J/cm³, which corresponds to a demagnetizing factor of about 10%. In a previous study, demagnetizing factors for thin epitaxial Er superlattices were as low as 30%, so this value is reasonable. Moreover, the calculated latent heat is $2.70 \pm 0.34\,\text{J}/\text{cm}^3$, which agrees well with the value of $2.74 \pm 0.07\,\text{J}/\text{cm}^3$, obtained in recent experiments on bulk Dy [15] by Gschneidner and co-workers. Additionally, the entropy difference $0.046 \pm 0.005\,\text{J}/\text{cm}^3/\text{K}$ lies reasonably close to the measured $0.030 \pm 0.001\,\text{J}/\text{cm}^3/\text{K}$ [15]. This establishes that the fitting parameters are physically-reasonable.

c-axis-oriented Dy. Since the magnetic moments are constrained to lie in the plane of the film, there is no contribution from shape anisotropy. The calculated latent heat and entropy difference are also in good agreement with experiment.

Bulk Dy under uniaxial stress, cubic sample. The calculated shape anisotropy is nearly negligible, which may point to the importance of domains in this sample. For the case of uniaxial pressure along $[11\bar{2}0]$, the data could be fit only by assuming that the easy magnetization axis rotates into the four remaining $[11\bar{2}0]$ directions. In the original uniaxial pressure experiments this change in easy magnetization axis was not detected, so that the present research with thin films makes an important clarification of this early work.

Bulk Dy under uniaxial stress, spherical sample. No reasonable fitting parameters could be obtained for the case of uniaxial pressure along $[11\bar{2}0]$. Given the large disparity between

the data obtained for the cubic and spherical samples, however, this may point to measurement inaccuracies.

Bulk Dy under hydrostatic stress. The calculated exchange energy is $E_{EX} = -0.22\boldsymbol{e}_{11} \, \text{J}/\text{cm}^3$, which is of opposite sign to the other calculated exchange energies. This appropriately reflects that the difference in magnetoelastic energy increases with increasing hydrostatic pressure, but that the transition temperature correspondingly decreases.

Sample	E_{EX}	$E_S\varepsilon_{11}$	ΔS	ΔE_0
	J/cm³	J/cm³	J/cm³/K	J/cm³
b-axis	0.30	-0.35[a]	0.046 ± 0.006	2.70 ± 0.34
c-axis	0.10	0	0.032 ± 0.009	2.25 ± 0.64
bulk, cube, P‖a	0.05	0	0.049 ± 0.006	4.25 ± 0.55
bulk, cube, P‖b	0.38	0	$0.028 \pm .003$	2.45 ± 0.29
bulk, cube, P‖c	0.14	-0.10	0.022 ± 0.009	2.02 ± 0.78
bulk, sphere, P‖a	n.a.	n.a.	n.a.	n.a.
bulk, sphere, P‖b	0.30	-1.0	0.047 ± 0.02	5.26 ± 2.1
bulk, sphere, P‖c	0.29	0	$.018 \pm .005$	1.60 ± 0.44
bulk, hydrostatic	-0.22	-1.0	0.027 ± 0.0005	2.42 ± 0.03

[a] In b-axis-oriented Dy shape anisotropy applies only to compressive strain, when the moments have a component normal to the film plane.

Table 5.3. The results of fitting the calculated magnetoelastic energy and measured T_C to the model discussed in the text.
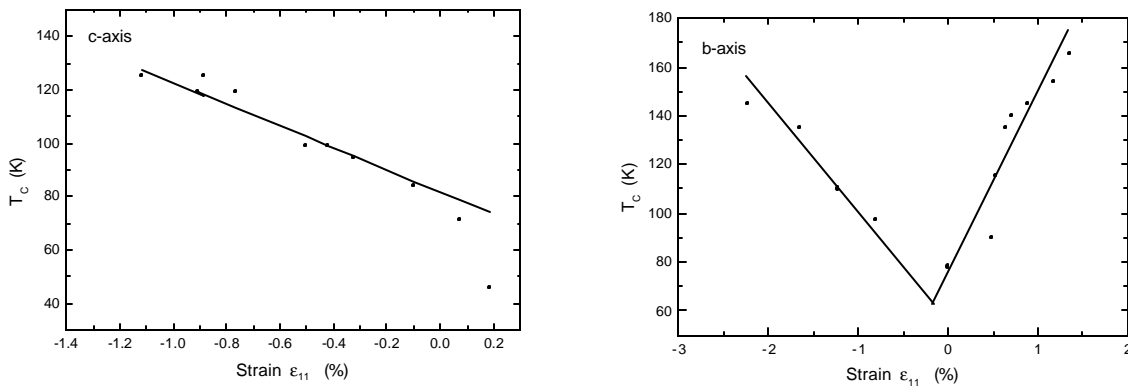

Figure 5.6. The calculated T_C for c-axis-oriented Dy (left) and b-axis-oriented Dy (right). The solid line is a fit to the data using the model discussed in the text.
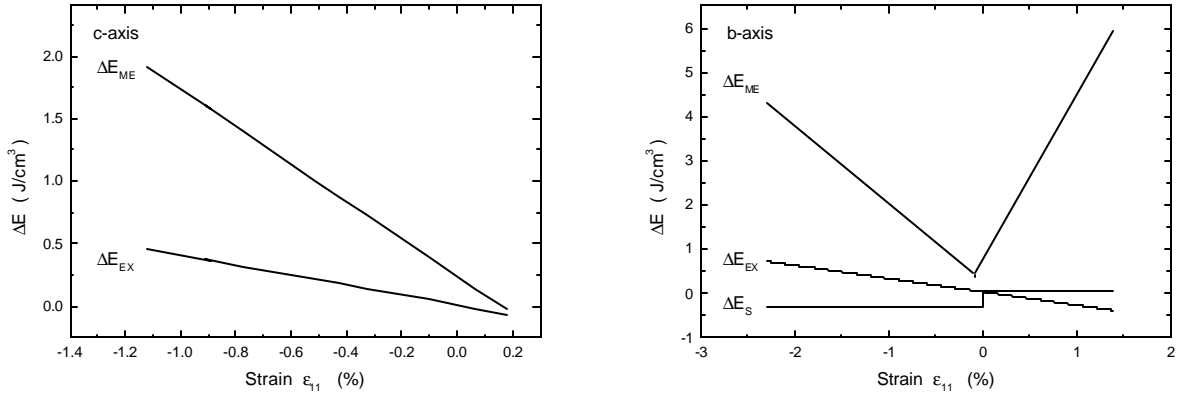
Figure 5.7. The best fitting energy difference ($\Delta E = E_{FM} - E_{AF}$) for c-axis-oriented Dy (left) and b-axis-oriented Dy (right). For compressed b-axis-oriented Dy, shape anisotropy is an additional term.

Figure 5.8. The calculated T_C for bulk Dy under under hydrostatic pressure. The solid line is a fit to the data using the model discussed in the text.

In summarizing this calculation it is noted that the phase transition is first order and the transition temperature T_C depends linearly on the differences of internal energies for the ferromagnetic and antiferromagnetic phases. Reasonable values of the exchange energy, shape anisotropy, latent heat and entropy change are obtained when the model is fit to the T_C vs. strain data for both b-axis- and c-axis-oriented Dy, and for bulk Dy under both uniaxial and hydrostatic strains. Three key results of this analysis are 1) the shape anisotropy corresponds to a demagnetizing factor of 10% for b-axis-oriented Dy, and this points to the importance of domain effects on the observed ferromagnetic ordering; 2)

analysis of published data for bulk Dy under uniaxial strain shows that the sample magnetizes along *different* [11$\overline{2}$0] axes, depending on whether the strain is applied parallel to the *a* or *b* axes; and 3) shape anisotropy plays a negligible role for bulk samples.

5.4 Expected Magnetostriction

Chapter 1 reviews the behavior of the ferromagnetic transition in bulk Dy in zero field. The transition is accompanied by a spontaneous orthorhombic distortion with approximate strains $\Delta a/a$=+0.2%, $\Delta b/b$=-0.5%, $\Delta c/c$=+0.3%, as shown in Figure 5.9. Beach and co-workers found that despite epitaxial clamping c-axis-oriented Dy is nevertheless able to undergo a similar orthorhombic distortion by breaking into domains for which the average strain is zero. This was recently studied in more detail by O'Donovan, who found that the distortion is first observable at temperatures somewhat lower than T_C, and that the distortion slowly grows in magnitude as the temperature is reduced [16]. A mechanism whereby the epitaxial clamping constraint can be overcome by an appropriate domain structure was proposed by Tsui and Flynn [14].

Unfortunately, measurements of the lattice constants of b-axis-oriented Dy as a function of temperature are not yet available. However, the mathematical framework developed in Section 5.3 permits calculation of the expected magnetostriction. At any temperature above or below T_C the sample must be in equilibrium, so the derivative of Eq. (5.2) with respect to the equilibrium strains must vanish. Since the film is clamped to the substrate, this gives

$$\Delta e_{22} = (K_{22}^{FM} - K_{22}^{AF}) / c_{11} \tag{5.6}$$

where K_{22}^{FM} and K_{22}^{AF} are the magnetoelastic coefficients in the ferromagnetic and antiferromagnetic states, respectively. For the case of stretched b-axis-oriented Dy, substitution of the values of Table 5.1 and 5.2 gives $\Delta e_{22} = -0.37\%$. This is a compression

along the out-of-plane b-axis, but of lesser magnitude than the value for bulk Dy. For the case of compressed b-axis-oriented Dy, this gives $\Delta e_{22} = +0.053\%$, which is a small expansion. Because the film is clamped in the two in-plane directions, these strains are equal to the volume dilatation which accompanies the transition.

This behavior is sketched in Figure 5.9. Because of epitaxial clamping the different polarizations which are each possible in the stretched and compressed cases will give rise to identical magnetostrictions. Precise measurements of the magnetostriction of epitaxial Er are currently being conducted by C. Durfee; this work may eventually be extended to include b-axis-oriented Dy.

AF, T > T_r   FM, T < T_r

a > a_v   a > a_iv

TENSILE STRAIN

AF, T > T_c   FM, T < T_c

a < a_v   a < a_ii
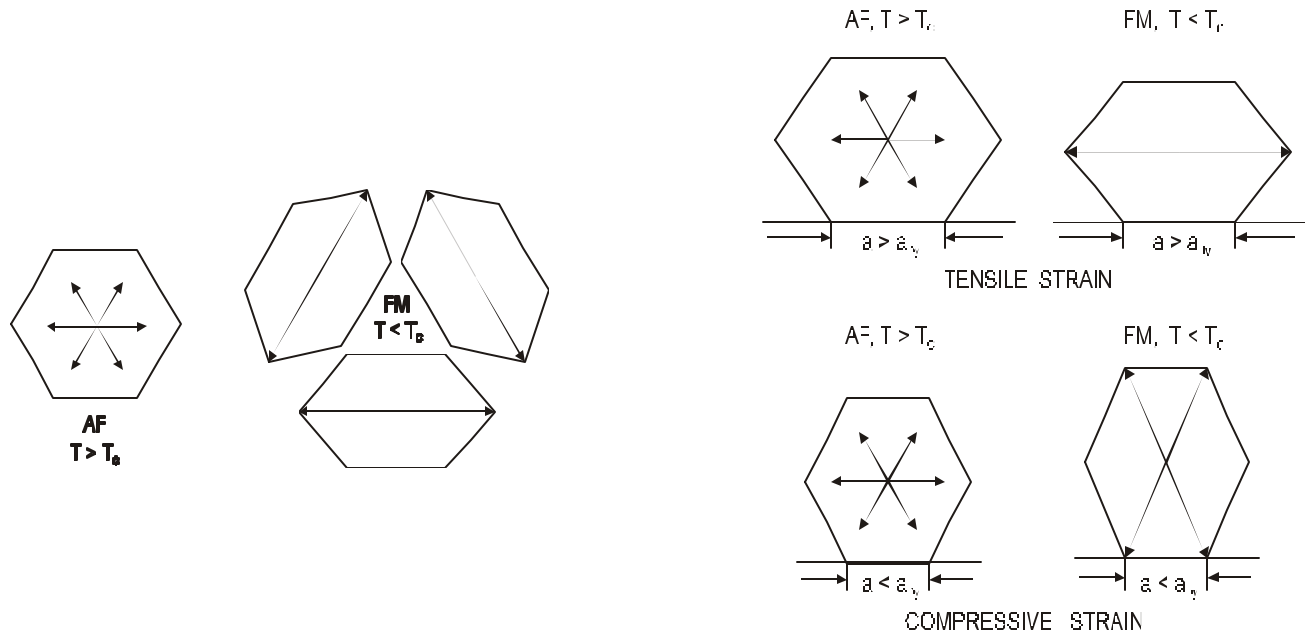
COMPRESSIVE STRAIN

AF
T > T_s

FM
T < T_s

Figure 5.9. The orthorhombic distortions, shown exaggerated, which accompany the ferromagnetic transitions in bulk Dy (left) and those expected for b-axis-oriented Dy (right).

5.5 The Critical Field, H_C

An abrupt inflection or change in slope of M vs. H can be seen in Figures 4.3 and 4.7 of Chapter 4 between T_C and T_N, when the b-axis-oriented Dy samples are antiferromagnetic. This kink occurs at a specific critical value H_C of the applied field. Two important observations are 1) the critical field is almost independent of temperature and, in contrast to both bulk and c-axis-oriented Dy, does not vanish as T approaches T_C; and 2) the critical field depends on strain. This Section interprets the behavior using the theory developed for critical fields in bulk Dy.

The nature of the critical field in bulk Dy was reviewed in Chapter 1. The phase diagram shown as Figure 1.14 indicates that an applied field can force the material into either a ferromagnetic state or a fan state, depending on the temperature and the field strength.   It is obvious that H_C must depend on the magnetic anisotropy, but the temperature dependence is less clear. This phase diagram was first explained in a series of calculations by Nagamiya, Kitano, and co-workers who showed that the critical field depends on the strength of the basal plane magnetocrystalline parameter K_6^6 [17],[18],[19]. Since this parameter depends weakly on temperature, the critcal field H_C also depends on temperature; the relationship between the two is made clear by the reduced phase diagram, shown as Figure 1.15.

In Section 5.2 it is shown that, in addition to the usual magnetocrystalline anisotropy, shape and magnetoelastic anisotropy make important contributions to the total basal plane anisotropy of b-axis-oriented Dy.   Although a rigorous mathematical description is lacking for b-axis-oriented Dy, H_C clearly must depend not only on magnetocrystalline anisotropy K_6^6 but also on the magnetoelastic and shape anisotropies. Since these additional terms are large and temperature-independent, it therefore follows that H_C must not depend strongly on temperature.

The magnitude of the combined magnetoelastic and shape anisotropy contribution can be estimated from the depth of the energy barriers for a magnetic moment as it is rotated in-plane, as shown in Figure 5.1. The energy barriers for compressed, unstrained, and stretched b-axis-oriented Dy are larger than the bulk value by a factor of 3, 5, and 9,

respectively. Thus, regardless of the state of the strain, magnetoelastic effects in thin b-axis Dy increase the usual magnetocrystalline anisotropy by a significant and temperature-independent amount.   This provides a qualitative explanation for the observed temperature-independence of H_C.

Unfortunately, the additional anisotropic terms for b-axis-oriented Dy are not included in the Hamiltonian of Eq. (1.31) and therefore Eq. (1.33) cannot be used to predict the strain dependence of H_C. Qualitatively, however, Eq. (1.32) shows that the basal plane anisotropy reduces the critical field, so that the increasing anisotropy demonstrated in Figure 5.1 above for compressed, unstrained, and stretched Dy suggests that the critical field should decrease as the strain changes from compressive to tensile. This is precisely what is observed in Figure 4.7. The in-plane [$11\overline{2}0$] axis becomes an increasingly easy magnetization axis for tensile strain, so a progressively smaller applied field is required to force magnetization in this direction.

Note that there nevertheless remains some small temperature dependence of H_C. It is reasonable that this is due to a small magnetoelastic contribution to H_C which derives from any small temperature dependence of the elastic constants, and possibly thermal expansion of the substrate and the epitaxial clamping.

5.6 Domain Walls and Domain Wall Pinning

The coercive fields for b-axis-oriented Dy are reported in Figure 4.13 of Chapter 4. The coercive field increased with increasing compressive strain, and it remains roughly constant for all values of tensile strain. This Section first addresses a possible magnetic domain structure in b-axis-oriented Dy, and it then interprets the observed coercivities in the context of the calculation by Egami and Graham that are reviewed in Section 1.4.

Magnetic Domains

Chapter 1 discussed that a magnetic system can lower its overall free energy by breaking into a collection of spatially-discrete but dipole-coupled domains, in which each is

uniformly magnetized. It is clear that there must be magnetic domains in the b-axis-oriented Dy samples since, although the samples are ferromagnetic below T_C, measurements of magnetization in zero applied field show negligible net moments. The magnetizations of bulk samples therefore grow by domain wall movement or by a combination of domain growth and coherent rotation of moments in a domain. The existence and motion of domain walls gives rise to non-zero coercive fields which derive from two basic mechanisms associated with domain walls: intrinsic coercive fields and coercive fields due to domain wall pinning.
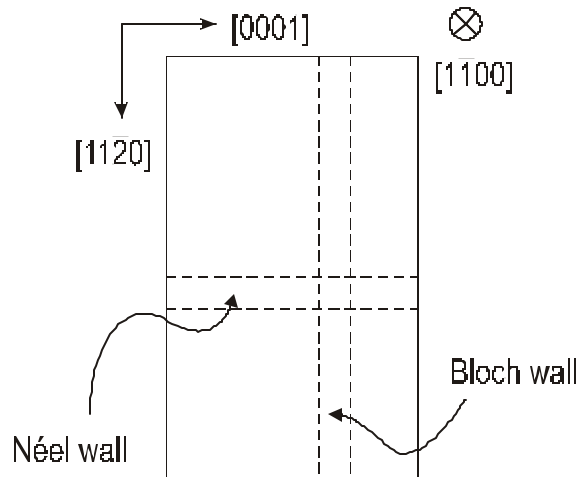

Figure 5.10. The simplest domain structure possible in b-axis-oriented Dy. The 180º Bloch and Néel walls are parallel to the [1120] and [0001] directions, respectively. Not shown are edge domains, which may exist to reduce magnetic poles at the surface.

Unfortunately, experimental measurements of the domain walls b-axis-oriented Dy are lacking [20], [21]. Nevertheless, a possible domain structure appears as Figure 5.10. The strong exchange coupling in the basal plane (even in the AF state, the basal plane is ferromagnetic) suggests 180º domain walls run parallel to the (0001) basal planes. The magnetization can freely rotate *between* basal planes and thus these are likely to be Bloch walls (with the axis of rotation perpendicular to the domain wall). Domains walls parallel to $(11\bar{2}0)$ are less likely, due to strong basal plane ferromagnetic coupling, but these may also exist [22].

Domain Wall Pinning

Section 1.4 reviews a calculation by Egami and Graham of the energetics of 180⁰ basal-plane domain walls in Dy. These authors showed that such domain walls give rise to an intrinsic coercive field of about 1 kOe which depends on exchange, magnetocrystalline, and magnetoelastic anisotropies [23],[24].

For comparison, the coercive fields for b-axis-oriented Dy are considered at the lowest measured temperature, since the calculation of Egami does not include the effects of temperature. For tensile strain the agreement between the calculation discussed in Section 1.4 and the experimental result of about 1 kOe, shown in Figure 4.13, suggests the observed coercivities are an intrinsic effect caused by domain walls. For b-axis-oriented Dy grown under compressive strain, however, the observed coercive fields are larger than calculated.

At issue is whether this increase is due to the intrinsic coercive force, or else due to pinning of domain walls by an external mechanism. As indicated by the difference between the solid curve and the dotted line of Figure 1.16, the structure of the domain wall is established principally by the strong exchange coupling term with $S^2 J_{i,i\pm1}$ = 170 K and $S^2 J_{i,i\pm2}$ = -46 K. The additional magnetocrystalline energy with K_6^6 = -2.5 K and magnetoelastic anisotropies with $B^g e^g$ = -4.0 K are a small perturbation on this term [23]. As shown in Figure 5.1 for b-axis-oriented Dy, the additional shape and magnetoelastic anisotropy are still small in comparison to the stronger exchange mechanism. Thus, the magnitude of the coercive field calculated by Egami should not be greatly altered in b-axis-oriented Dy.

Moreover, as can be seen in Figure 5.1, b-axis-oriented Dy under tensile strain has two stable configurations: alignment parallel and antiparallel to the in-plane [11$\overline{2}$0] axis in the respective cases. b-axis-oriented Dy under compressive strain has four additional stable states of minimum energy, and the energy barriers between these states are greatly reduced with respect to those for tensile strain. As a result, the expected modification of

the coercive field calculation from the values of Egami should yield, if anything, slightly higher coercive fields for the case of tensile rather than compressive strain [23], which is the opposite of that observed.

This analysis shows the increase of coercive field with increasing compressive strain is not likely to be an intrinsic effect of magnetic domains in thin films. The existence of an alternative domain configuration provides one possible resolution to the problem. It is known that the nucleation and growth of 90º edge domains is an important mechanism in the magnetization of thin films [25]. Unfortunately, experimental measurements of domain walls in b-axis-oriented Dy are lacking.

It is also possible that the increase of coercive field with increasing compressive strain may arise from a domain wall pinning mechanism. A numerical model which provides some evidence corroborating this is presented in Chapter 6. From a structural viewpoint, however, no evidence suggests that compressively-strained Dy samples on Lu-rich buffers are less structurally perfect than their tensile counterparts grown on Y-rich buffers. Lu, with slightly better lattice misfit, nucleates on Zr, whereas Y does not. In fact, the narrowest transverse x-ray linewidth of 0.3º was obtained for the most compressively-strained sample of Dy on pure Lu. Reversed domains near an imperfection may contribute to domain wall motion [26]; such imperfections may expedite as well as impede magnetization reversal [27], and therefore greater imperfection density may exist in samples exhibiting smaller coercive fields [28]. The ultimate understanding of the high coercive fields may have to await measurements of domain walls and domain wall nucleation and growth.

5.7 Néel Temperature

In Chapter 4 the Néel temperatures are identified in the *M(T)* data in Figure 4.1 by the cusp in the susceptibility, and it was found to be about 165 K for all samples, with no discovered systematic variation with strain or other parameters. This value lies below the result of T_N = 178 K observed for bulk Dy and for c-axis-oriented thin films and

superlattices. Further measurements presented in Figure 4.12 show that T_N decreases with decreasing film thickness, with T_N = 178 K, 172 K, and 165 K for 100 nm, 50 nm, and 7 nm thicknesses, respectively.

The Néel temperature in magnetic thin films have long been observed to decrease with decreasing thickness in this way [29]. In particular, this happens in polycrystalline Dy thin films [30], and in epitaxially-grown Er films and superlattices [12]. In the latter case, the magnitude of the effect (5 K) was less than that observed here for b-axis-oriented Dy (13 K). This effect has been studied theoretically for Ising films by Fisher [31],[32]. More generally, it is attributed to two causes: 1) the increased role of fluctuations or disorder as the dimensionality is reduced; and 2) the reduction in the volume defined by the magnetic coherence length.

One obvious mechanism for the reduction of magnetic coherence is reduced structural coherence. This could be the result of roughness or interdiffusion. While not entirely ruled out, neither effect is unlikely. Regarding *roughness*: AFM measurements shown in Figure 3.22 give surface roughness which are not unreasonable for epitaxial films. Further, as reported in Chapter 3, the mosaicities of these samples are as low as 0.3⁰, comparable with many c-axis-oriented samples. No change in T_N was observed for b-axis-oriented Dy samples of equal thickness despite changes of mosaic from 0.3⁰ to 0.7⁰. Regarding *interdiffusion*: First, the growth temperature was selected to specifically avoid interdiffusion. Second, there was a wide variance in the times required for sample growth; early samples had six layers of Dy, but later samples were grown more quickly, and with only five layers. Were the temperature near an interdiffusion threshold, the difference in growth times would appreciably affect T_N, which was not observed. Third, hysteresis loops showed clear evidence for near saturation at high applied fields, suggesting a minimum of Dy moments trapped at the interfaces.

It is possible that the observed reduction in T_N, which is greater than seen in c-axis-oriented Dy or Er, is due to a modification of the exchange coupling due to the finite thickness of the samples. The connection between T_N in bulk rare earths (neglecting anisotropy) and the exchange interaction $J(\mathbf{Q})$ is [33],

$$T_N = 2J(\mathbf{Q})\frac{S(S+1)}{2k_B} \qquad (5.7)$$

The modification of $J(\mathbf{Q})$ in thin film Dy has been discussed previously by Tsui [34]. For c-axis-oriented Dy, the spatial form of $J(R)$ stays the same as shown (see Chapter 1) for bulk rare earths. For b-axis-oriented Dy, however, the exchange interaction along $\mathbf{b}$ becomes

$$J(R) = \sum_{q,R_a,R_c} J(q)\exp(-i\mathbf{q}\cdot\mathbf{R} + iq'_{c*}R_c)$$
$$= \sum_{q_{a*}} J(q_{a*},0,q')\exp(-iq_{a*}R) \qquad (5.8)$$

The summation misses the peak in $J(\mathbf{Q})$ along $\mathbf{c}$, and this results in a further reduction of the RKKY interaction, in addition to its already short range.

Interestingly, further studies of b-axis-oriented rare earth thin films of varying thickness, including measurements of the AF periodicities, may eventually provide a useful way to study the length scale of magnetic coupling, particularly in the planar ferromagnets such as Dy, Tb, and Ho.

5.8 The Possible Occurrence Quantum Tunneling

Chapter 4 presents low-temperature magnetic viscosity measurements for two samples, one with compressive strain (ε_{11}=-1.66%) and one with tensile strain (ε_{11}=+0.89%). The samples were cooled in zero field to a selected temperature, a 1 T field was applied, and magnetization data were collected as a function of time for up to seven hours thereafter. Two key observations were made: 1) the viscosity decreases with decreasing temperature until about 10 K, below which the viscosity is constant or slightly increasing, which identifies two temperature regimes with distinct kinetic processes; and 2) T_c^* was found to be independent of strain.

Both the non-zero intercept at zero-temperature and the abrupt change in slope suggest that $T_c^* = 10$ K is a crossover temperature from thermal activation (TA) to quantum

tunneling (QTM). For lower temperatures, the transitions between magnetic states may occur via quantum tunneling. Interestingly, in 1971 Egami cited evidence for quantum tunneling of Bloch walls in Dy [35],[36]. There the magnetization rate of bulk Dy was studied in fields between 10^2 and 10^3 Oe and was found to be temperature-independent below 10 K; the data are shown as Figure 5.11.

Some factors cast doubt on this conclusion. First, QTM has recently been observed in a number of systems, including simple magnets such as $Fe(CO)_5$ and $Tb_{0.5}Ce_{0.5}Fe_2$, magnetic multilayers of FeSm, DyCu, FeCu, and complicated, organic molecular magnets [37],[38],[39],[40],[41]. The present crossover temperature of $T_c^* = 10$ K is higher than that reported for these systems which are typically 3 K or much less [37].

Second, with regard to the present results, the magnetic viscosity is not strictly temperature-independent below T_c^*, but in fact *increases* slightly with decreasing temperature. Quantum tunneling processes may exhibit a weak temperature dependence, due to dissipation, but the usual dependence on temperature is the opposite of that observed [42],[43].

Third, a detailed theory of domain wall tunneling in Dy followed the report by Egami. The effective mass of a Bloch wall was calculated in the random-phase approximation, and the WKB formalism was used to obtain the tunneling rate [44]. The quantitative conclusion was that the crossover temperature to the tunneling regime should be 1 K, significantly less than observed.

An alternative to QTM is the possibility that the relaxation studies for b-axis-oriented Dy have identified a new ordering process that is not well-studied in rare earth thin films. Most studies involving Dy to date have focused on temperatures above 10 K, and recent reports using higher-purity Dy show phase behavior which differs significantly from previous measurements [15]. A recent article reports magnetic ordering in bulk Dy at 4 K [45] in which Dy acquires a small component of magnetization along the [0001] axis. Since the temperature-dependence of the magnetoelastic constants in Dy are well-understood, this process (if confirmed) is very difficult to understand.

Conclusions drawn from the low temperature magnetic relaxation data may be summarized as follows. Abrupt changes in ordering kinetics at 10 K in a 1 T field are observed in compressed and stretched b-axis-oriented Dy. These agree with similar crossovers at 10 K observed by Egami in bulk Dy with smaller fields, establishing both that the mechanism is independent of strain and not strongly dependent on applied field below 1 T. Current research in progress by C. Durfee may illuminate the nature of tunneling phenomena in the rare earths.
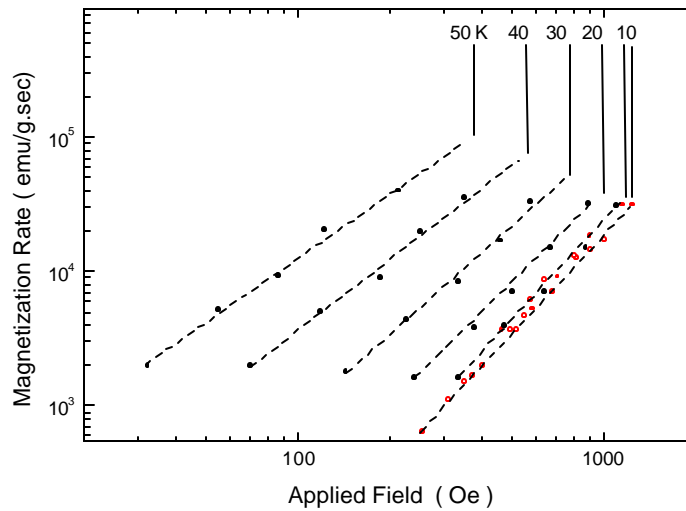

Figure 5.11. The temperature and applied field dependence of the magnetization rate in bulk Dy. After Reference [35]. Below 10 K, the rate is constant.

5.9 Summary

This Chapter provides interpretations of the results presented in Chapter 4. The specific conclusions are as follows: 1) The observed dependence of the easy axis of magnetization on strain is reproduced by calculations of the anisotropy using the full magnetoelastic Hamiltonian. 2) The ferromagnetic/antiferromagnetic phase transition was studied using a phenomenological model with magnetoelastic parameters obtained from bulk Dy and applied to b-axis-oriented, c-axis-oriented and bulk Dy. The driving energy favoring

ferromagnetism was found to vary linearly with strain. A model which connects the Curie temperature linearly with driving energy was proposed. A fit to measured T_C using this model gave reasonable values of the parameters. The behavior of both epitaxial and bulk Dy could thus be explained by a single model. 3) The measured coercive fields were examined and for the case of tensile strain, the coercive field strength is found to agree with the calculations of Egami. Close examination of the Egami calculation suggests that domain wall pinning increases with increasing compressive strain. 4) The critical field H_C is temperature-independent. For bulk Dy, the temperature dependence of H_C derives from the temperature dependence of the magnetocrystalline anisotropy constant, $K_{6,6}$. In the case of b-axis-oriented Dy, the additional effects of magnetoelastic coupling and shape anisotropy introduces large, temperature-independent additions. 5) The reduction in Néel temperature for b-axis-oriented Dy, and its systematic variation with strain may be caused by a reduction of the magnetic coherence length in the strongly-ordering (0001) planes that occurs in the b-axis-oriented geometry. 6) The change of magnetic relaxation data below 10 K signifies a crossover between different regimes of magnetic ordering but the data do not establish whether or not this is quantum tunneling.

References

[1] Since the crystal field can only couple to the charge degrees of freedom, the dominant contribution of the spin-orbit coupling in the rare earths ensures here that the spins are coupled specific crystallographic directions.

[2] F. J. Darnell, E. P. Moore, *J. App. Phys.* **34**, 1337-1338 (1963).

[3] B. R. Cooper, *Phys. Rev.* **169**, 281-294 (1968).

[4] B. R. Cooper, *Phys. Rev. Lett.* **19**, 900-903 (1967).

[5] W. E. Evenson, S. H. Liu, *Phys. Rev.* **178**, 783-794 (1969).

[6] K. Dumesnil, C. Dufour, Ph. Mangin, G. Marchal, *Phys. Rev. B* **53**, 11218-11221 (1996).

[7] For an authoritative review, see C. P. Flynn, M. B. Salamon, in *Handbook on the Physics and Chemistry of Rare Earths,* K. A. Gschneidner, L. Eyring, eds. (Elsevier, Amsterdam, 1996), 1.

[8] M. Mori, Y. Tsunoda, *J. Phys. Condens. Matter* **5**, L77-L84 (1993).

[9] R. W. Erwin, J. J. Rhyne, M. B. Salamon, J. Borchers, S. Sinha, R. Du, J. Cunningham, C. P. Flynn, *Phys. Rev. B* **35**, 6808-6825 (1987).

[10] R. W. Erwin, J. J. Rhyne, M. B. Salamon, R. Du, C. P. Flynn, in *Mat. Res. Soc. Symp. Proc. Vol. 166*, S. M. Shapiro, S. C. Moss, J. D. Jorgensen, eds. (MRS, Pittsburgh, 1990).

[11] A. del Moral, in *Magnetoelastic effects and applications*, L. Lanoutte, ed. (Elsevier, Amsterdam, 1993).

[12] J. Borchers, Ph.D. thesis, University of Illinois, 1990.

[13] T. Egami, *J. Phys. C* **5**, L85-88 (1972).

[14] F. Tsui, C. P. Flynn, *Phys. Rev. Lett.* **71**, 1462-1465 (1993).

[15] K. A. Gschneidner, Jr., V. K. Pecharsky, D. Fort, *Phys. Rev. Lett.* **78**, 4281 (1997); V. K. Pecharsky, K. A. Gschneidner, Jr., D. Fort, *Scripta Mater.* **35**, 843-848 (1996).

[16] K. O'Donovan, M. B. Salamon, C. P. Flynn, preprint.

[17] For an excellent review of this work, see B. Coqblin, *The electronic structure of rare-earth metals and alloys: the magnetic heavy rare-earths* (Academic Press, London, 1977).

[18] B. R. Cooper, in *Magnetic properties of the rare earth metals*, R. J. Elliott, ed. (Plenum, London, 1972).

[19] T. Nagamiya, *Solid State Physics*, vol. 20 (Academic, London).

[20] Magnetic force microscopy could be used, in principle, to make such measurements, but the available MFM apparatus at the University of Illinois does not have a low-temperature stage necessary to achieve a ferromagnetic state.

[21] See, for example, R. Carey, E. D. Isaac, *Magnetic domains and techniques for their observation* (Academic Press, New York, 1966).

[22] E. A. Nesbitt, J. H. Wernick, *Rare earth permanent magnets* (Academic Press, New York, 1973).

[23] T. Egami, C. D. Graham, *J. App. Phys.* **42**, 1299-1300 (1971).

[24] T. Egami, in *Proceedings of the 17th Annual conference on magnetism and magnetic materials, No. 5* (American Institute of Physics, New York, 1972).

[25] R. F. Soohoo, *Magnetic thin films* (Harper & Row, New York, 1965).

[26] D. J. Craik, R. S. Trebble, *Ferromagnetism and ferromagnetic domains* (Wiley, New York, 1965).

[27] R. S. Trebble, *Magnetic domains* (Methuen, London, 1969).

[28] F. Brailsford, *Magnetic materials* (Methuen, London, 1948).

[29] See, for example, D. Kostyk, Y. Shapira, E. J. McNiff, T. Q. Vu, A. Twardowski, *Sol. State Comm.* **92**, 473-476 (1994), and references therein.

[30] J. Dudas, A. Feher, S. Janos, *Acta Phys. Pol.* **A72**, 263-265 (1987).

[31] M. E. Fisher, *Phil. Mag.* **7**, 1731 (1962).

[32] M. E. Fisher, in *Critical phenomena*, M. S. Green, ed. (Academic, New York, 1971).

[33] B. Coqblin, *The electronic structure of rare-earth metals and alloys: the magnetic heavy rare-earths* (Academic Press, London, 1977), p. 127.

[34] F. Tsui, C. P. Flynn, M. B. Salamon, R. W. Erwin, J. A. Borchers, J. J. Rhyne, *Phys. Rev. B* **43**, 13320 (1991).

[35] T. Egami, *Phys. Stat. Sol.* **A20**, 157-165 (1973).

[36] T. Egami, *Phys. Stat. Sol.* **B57**, 211-224 (1973).

[37] L. L. Balcells, X. X. Zhang, F. Badia, J. M. Ruiz, C. Ferraté, J. Tejeda, *J. Mag. Mag. Mat.* **109**, L159-L163 (1992).

[38] E. M. Chudnovsky, L. Gunther, *Phys. Rev. Lett.* **60**, 661-664 (1988).

[39] D. D. Awschalom, M. A. McCord, G. Grinstein, *Phys. Rev. Lett.* **65**, 783-786 (1990).

[40] E. M. Chudnovsky, Science **274**, 938-939 (1996).

[41] D. D. Awschalom, J. F. Smyth, G. Grinstein, D. P. DiVincenzo, D. Loss, *Phys. Rev. Lett.* **68**, 3092 (1992).

[42] A. Garg, G. Kim, *Phys. Rev. Lett.* **63**, 2512-2515 (1989).

[43] The most complete work in this area is D. Waxman, A. J. Leggett, *Phys. Rev. B* **32**, 4450-4468 (1985). For an outstanding discussion of tunneling rates using a path integral approach, see E. M. Chudnovsky, *Phys. Rev. B* **54**, 5777-5783 (1996).

[44] T. Egami, *Phys. Stat. Sol.* **A19**, 747-758 (1973).

[45] F. Willis, N. Ali, *J. App. Phys.* **69**, 5694-5696 (1991).